Continuum Mech. Thermodyn. (2019) 31:1035–1050
https://doi.org/10.1007/s00161-018-0710-2

ORIGINAL ARTICLE

Kamel Berkache · Sai Deogekar · Ibrahim Goda · R. Catalin Picu · Jean-François Ganghoffer

Identification of equivalent couple-stress continuum models for planar random fibrous media

Received: 14 January 2018 / Accepted: 3 September 2018 / Published online: 24 September 2018

Abstract The purpose of this paper is to develop a homogeneous, couple-stress continuum model as a representation of 2D random fiber networks in the small deformation regime. The couple-stress substitution continuum is calibrated based on the response of a network model (window of analysis, WOA) subjected to prescribed kinematic boundary conditions applied on part of the WOA boundary, while the free surface boundary conditions are applied on complementary surfaces. Each fiber in the network is considered as a Timoshenko beam and the cross-links between fibers are modeled as welded joints in which the relative angles between the crossing beams remain constant during deformation, and hence they transmit moments along and between crossing fibers. The effective elastic constants of the couple-stress continuum are deduced by an equivalent strain energy method, and the characteristic lengths are identified from the resulting homogenized moduli. The competition between the affine (ADR) and non-affine (NADR) deformation regimes is shown to be quantified by the bending length, a scalar quantity that measures the relative importance of fiber bending in comparison with fiber stretch. The scaling laws of the effective moduli versus the bending length, network density and window size are determined in the affine and non-affine deformation regimes. The motivation of the adopted couple-stress substitution continuum is brought by comparing the identified effective non-classical properties with the mechanical properties predicted by FE simulations performed over the fully resolved fibrous network.

Keywords Couple-stress continuum · Random fibrous networks · Homogenization · Finite element method

Communicated by Francesco dell'Isola.

K. Berkache
Department of Energetic and Fluid Mechanics, Faculty of Physics, USTHB, POB 32, El-Alia, Bab-Ezzouar, 16111 Algiers, Algeria
E-mail: kamelberkache@hotmail.com

I. Goda
LPMT, Université de Haute-Alsace, 11 rue Alfred Werner, 68093 Mulhouse Cedex, France
E-mail: ibrahim.goda@uha.fr

S. Deogekar · R. C. Picu
Department of Mechanical, Aerospace and Nuclear Engineering, Rensselaer Polytechnic Institute, Troy, NY 12180, USA
E-mail: deoges@rpi.edu

R.C. Picu
E-mail: picuc@rpi.edu

J.-F. Ganghoffer (✉)
LEM3, Université de Lorraine - CNRS, 7 rue Félix Savart, BP 15082, 57073 Metz Cedex 03, France
E-mail: jean-francois.ganghoffer@univ-lorraine.fr

1 Introduction

Many natural and synthetic materials exhibit fibrous microstructures. In nature, fibrous structures arrange in a hierarchic manner to form highly complex and multi-functional parts; protein frequently occurs in fibrous form. The most abundant fibrous protein in mammals is collagen which is a major constituent of tendons, ligaments and most of the organic matrix in bone and dentin [1]. Synthetic fibrous materials have high stiffness and strength-to-weight ratios, making them quite attractive in numerous applications such as fiber-reinforced composites, civil constructions and in the aerospace industry. (Interesting examples of fibrous complex structures are described in the works [2–5].) Hence, the study of fibrous networks is essential for characterizing the mechanical properties of such materials and understanding the dependence of these properties on structural parameters of the fibrous networks. Since material properties are strongly influenced by structural arrangement of constituent fibers, it is necessary to model the deformation and failure mechanisms on system subscale. Cox [6] calculated the elastic modulus of paper by assuming affine stretching of fibers as the dominant deformation mechanism. However, when fibers have a relatively low bending stiffness and are randomly oriented, bending is an important feature, particularly in absence of matrix which embeds the fibers [7,8]. Biopolymer network models studied in [9–11] elucidate the interplay between fiber stretching and bending in the overall nonlinear elastic behavior of the material at macroscale. As discussed in [12], models used to describe the mechanical behavior of fiber networks can be categorized as phenomenological models and homogenized models accounting for micromechanics at smaller scales. The phenomenological models rely on fitting a mathematical model to an experimental stress–strain curve to obtain the required model parameters. This approach does not capture the dependence of model parameters on structural properties of the fiber network. Homogenized models overcome this shortcoming by homogenizing fiber networks using analytical or computational methods. We shall mention in this category the contribution [13] in which the authors adopt a Lagrangian model à la Hencky for estimating elastic parameters starting from a geometrically nonlinear behavior of the fiber network. Indeed, homogenization techniques are very useful since effective continuum models have, in general, a low computational cost. Obviously, depending on the research topic, different methods can be applied. (See [14] for rigorous results about one-dimensional discrete dynamical systems, or [15] for some applications to inhomogeneous systems described as foams and [16] for homogenization of fiber-reinforced composites using asymptotic methods.)

A number of parameters, influencing the overall mechanical behavior of the material, are used to characterize a fiber network. An important structural descriptor is the network density, ρ, defined as the total fiber length per unit area. The orientation tensor, describing the alignment of fibers, is another factor influencing the material response of the network. Fiber properties are also important. Bending length of fibers, $l_b = \sqrt{EI/EA}$, quantifies the relative importance of bending stiffness of the fiber to its axial stiffness. (Here, E is the fiber elastic modulus, A is the cross-sectional area, and I is the moment of inertia of the fiber cross section.) A number of works have established that as the network density ρ and bending length l_b increase, the dominant fiber deformation mode transitions from bending to stretching and the degree of heterogeneity decreases [9,10,17,18]. Heterogeneity leads to a strong dependence of the apparent elastic moduli on the size of the probed network domain. The degree of heterogeneity is quantified in [18] by evaluating the correlation function between tensile modulus and size of the probed domain. Although there are several works in the literature based on the affine deformation assumption (such as [8] and [19]), many random fibrous networks deform non-affinely. Recent investigations in [20,21] concluded that non-affine deformation of random fibrous networks occurs at a lower energy level than affine deformation of the same structure and is dominated by bending of the fibers (since the bending modulus is much smaller than the stretching modulus). The stochastic generation of fibers is responsible for the formation of clusters of fibers, which in turn generate internal strain gradients corresponding to non-affine deformations of the fiber network even when the network is subjected to uniform far-field strain. Affine deformation regime refers to motion of internal nodes following the imposed boundary displacements, whereas non-affine deformation regimes occur when the internal nodes do not follow the imposed kinematic boundary conditions as shown in Fig. 1.

Our methodology in this work belongs to the class of homogenization approaches. In this work, we adopt the framework of generalized continuum theories, which have been used extensively to explain size effects for a wide class of materials, but not for random fibrous materials to our knowledge. This constitutes the main originality advocated so far in the present work. Classical continuum theory based on the Cauchy approach is the simplest continuum model in which the stress at a material point depends only on the strain at that point. As a consequence, it cannot incorporate microstructural size effects and internal, material-specific lengths. However, real heterogeneous materials exhibit internal length scales which are important to their mechanics and which

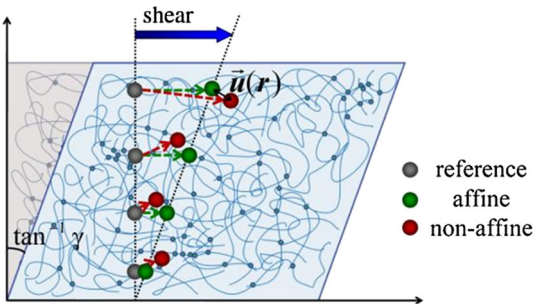

Fig. 1 Illustration of the difference between affine and non-affine deformation regimes

need to be accounted for in computational models, in order for these to be able to represent spatially varying strain fields. There are two main classes of generalized continuum theories: the first is called HIGHER- GRADE theories, in which the gradients of strains or the higher-order gradients of displacements are incorporated; the second class is called HIGHER- ORDER theories, in which additional degrees of freedom are incorporated. For more details about these two classes of theories, the reader is referred to Cihan [22], who presented a historical overview of generalized continuum theories. More complete descriptions of higher gradient continuum models can be found in [23–25]. Interesting applications of higher-order continuum theories are presented, instead, in the works [26–28]. The development of the nonlinear theory of elasticity traces back to the seminal work of Cosserat brothers [29]. At the beginning of the 1960s, several authors were interested in Cosserat's theories [30–35], and a special case of the Cosserat continuum theory has been investigated by Koiter [36], in which the microrotation of rigid triad is defined in terms of displacement gradients, known as couple-stress theory. In a recent work, Goda and Ganghoffer [37] identified the couple-stress moduli of vertebral trabecular bone by modeling the network of trabeculae as a porous material with an idealized periodic structure made of 3D open cubic cells. In this paper, we use the couple-stress theory as a modeling framework to identify both classical and non-classical moduli of two-dimensional random fiber networks, at the level of a window of analysis (WOA), and we analyze the influence of network parameters on the equivalent couple-stress moduli. Using energy equivalence, we systematically compute the full set of classical and non-classical moduli of the random fibrous networks. Similar methods have been used in [38] referred to granular systems, whereas in [39–42] various identification procedures have been applied to more geometrical structures.

The article is organized as follows: the identification of random fibrous networks is explained in Sect. 2. The method used for the identification of the couple-stress moduli based on the strain energy equivalence is presented in Sect. 3. The motivations for adopting an effective couple-stress model are exposed in Sect. 4. The influence of important network parameters, such as internal bending length, network density, size of WOA, on the computed effective mechanical moduli is studied in Sect. 5. Finally, a summary of the work is presented in Sect. 6 together with a few perspectives.

2 Generation of random fiber networks

Our random network consists of finite length fibers, with random orientation and random positions of their centers of mass. A number of geometrical characteristics of such random line networks are given in the work of Miles [43]. We consider here systems of two-dimensional networks in which the fibers are of identical length L_0 and are deposited on square regions of dimensions L as shown in (Fig. 2). In this work, we consider random structures to be a special class of stochastic fibrous networks and classify a random process as one where the events are independent of each other and equally likely, according to the criteria identified in one of the important works on modeling two-dimensional random fiber networks, Kallmes and Corte [44].

The mutual geometrical interaction of fibers provides the connectivity of the network; its non-uniformity can be captured by, for example, the variation of the fiber number density N (defined as the number of fibers per unit area) or the network density, $\rho = NL_0$ over different WOA's of size L in a bigger network. The cross-links are introduced at all points where fibers intersect; for these nodes, the coordination number (defined as the number of fiber segments converging at a node) is $2 \leq z \leq 4$ and they are modeled as "welded joints," which implies that both moments and forces are transmitted between the fibers in contact. The comparison of the impact of this choice of junction among other choices (rotating or pin) does not lead to noticeable differences

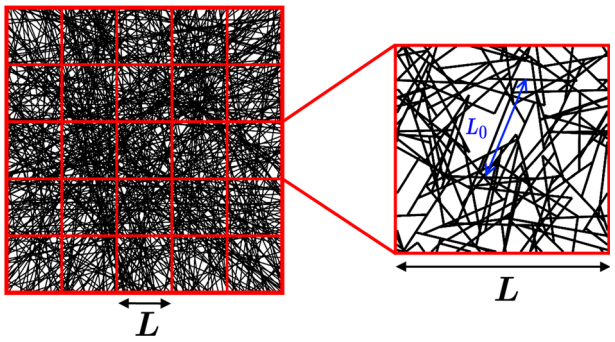

Fig. 2 Window of analysis (WOA) for a 2D Mikado network

in the effective mechanical response (for both the classical and non-classical moduli); numerical computations with "welded joints" type are more stable than those with "pin joints" type. The comparison between these types of joints is also discussed in [18].

3 Methodology for the identification of moduli based on couple-stress theory

In the micropolar theory, the deformation is described by the displacement vector $\boldsymbol{u}$ and an independent rotation vector $\boldsymbol{\phi}$, whereas in the more specific couple-stress theory, the rotation vector $\boldsymbol{\phi} = \phi \cdot \boldsymbol{e_z}$ in the present planar context is not independent of the displacement vector. (Here $\boldsymbol{e_z}$ is the unit normal vector to the plane of the network.) A special case of Cosserat theory is the couple-stress theory, in which the microrotation and macrorotation coincide [36]. In comparison with a classical continuum, a couple-stress continuum is obtained by adding a rotation (dependent of displacement vector) to each point of the continuum; it is based on the assumption that micromoments exist at each point of the continuum. The appealing aspect of the couple-stress theory is that a physically meaningful link can be made between the kinetic and kinematic variables of the couple-stress theory and the behavior of materials with microstructure like random fibrous networks. An extensive list of references to Cosserat and couple-stress elasticity models is available in the review articles by [45–48]. Considering the present 2D context, the microrotation is related to the displacement gradient by

$$\phi = \frac{1}{2}\left(\frac{\partial v}{\partial x} - \frac{\partial u}{\partial y}\right) \tag{1}$$

where $\boldsymbol{u} = [u, v]^T$ is the displacement field vector in 2D case. On the basis of the couple-stress theory in a 2D plane stress situation, the stress tensor has four independent components $\sigma_{xx}, \sigma_{yy}, \sigma_{xy}, \sigma_{yx}$ and the couple-stress tensor has two components m_{xz}, m_{yz}. The strain and microcurvature components can be expressed in terms of displacement gradients and microrotations as

$$\begin{aligned}
\epsilon_{xx} &= \frac{\partial u}{\partial x} \\
\epsilon_{yy} &= \frac{\partial v}{\partial y} \\
\epsilon_{xy} &= \frac{\partial v}{\partial x} - \phi \\
\epsilon_{yx} &= \frac{\partial u}{\partial y} + \phi \\
\kappa_{xz} &= \frac{\partial \phi}{\partial x} \\
\kappa_{yz} &= \frac{\partial \phi}{\partial y}
\end{aligned} \tag{2}$$

Introducing kinematic constraint (1) into the strain components defined in (2), the strain tensor ϵ_{ij} becomes symmetric with components defined as $\epsilon_{xy} = \epsilon_{yx} = \frac{1}{2}\left(\frac{\partial v}{\partial x} + \frac{\partial u}{\partial y}\right)$.

The static equilibrium in translation and rotation is given by

$$\begin{aligned}
\nabla \cdot \boldsymbol{\sigma} + \boldsymbol{f} &= 0 \\
\nabla \cdot \boldsymbol{m} - \boldsymbol{\varepsilon} : \boldsymbol{\sigma} + \boldsymbol{c} &= 0
\end{aligned} \tag{3}$$

Ignoring body forces $\boldsymbol{f}$ and body moments $\boldsymbol{c}$ in equation (3) leads to the set of equations

$$\begin{array}{l} \frac{\partial \sigma_{xx}}{\partial x} + \frac{\partial \sigma_{yx}}{\partial y} = 0 \\ \frac{\partial \sigma_{xy}}{\partial x} + \frac{\partial \sigma_{yy}}{\partial y} = 0 \\ \frac{\partial m_{xz}}{\partial x} + \frac{\partial m_{yz}}{\partial y} + \sigma_{xy} - \sigma_{yx} = 0 \end{array} \tag{4}$$

The last equation in (4) implies that the shear stress σ_{xy} differs from σ_{yx}; Mindlin [49] suggested then resolving σ_{xy} and σ_{yx} into a symmetric part σ_S and an anti-symmetric part σ_A

$$\sigma_S = \frac{1}{2}\left(\sigma_{xy} + \sigma_{yx}\right), \ \sigma_A = \frac{1}{2}\left(\sigma_{xy} - \sigma_{yx}\right) \tag{5}$$

The symmetric part of the shear stress produces the usual shear strain ϵ_{xy}, while the anti-symmetric part tends to produce a local rigid microrotation. Thus, the constitutive equation can be expressed in the following uncoupled form for the in-plane and out-of-plane bending responses (the fibrous microstructure is statistically endowed with centrosymmetry) as

$$\begin{Bmatrix} \sigma_{xx} \\ \sigma_{yy} \\ \sigma_S \\ m_{xz} \\ m_{yz} \end{Bmatrix} = \begin{bmatrix} \mathbf{A} & 0 \\ 0 & \mathbf{D} \end{bmatrix} \begin{Bmatrix} \epsilon_{xx} \\ \epsilon_{yy} \\ \epsilon_{xy} \\ \kappa_{xz} \\ \kappa_{yz} \end{Bmatrix} \tag{6}$$

With

$$\mathbf{A} = \begin{bmatrix} A_{11} & A_{12} & 0 \\ A_{12} & A_{22} & 0 \\ 0 & 0 & A_{33} \end{bmatrix}, \mathbf{D} = \begin{bmatrix} D_{11} & 0 \\ 0 & D_{22} \end{bmatrix} \tag{7}$$

Matrix $\mathbf{A}$ contains the classical Cauchy moduli relating stresses to strains, while matrix $\mathbf{D}$ contains the micropolar moduli relating the two couple-stress components of the present 2D description to the corresponding curvatures. We can derive the effective Young's moduli from the effective compliance matrix $[S] = [A]^{-1}$ as:

$$E_x = \frac{1}{S_{11}}; \ \ E_y = \frac{1}{S_{22}}. \tag{8}$$

Furthermore, the effective Poisson's ratios are computed as :

$$\nu_{xy} = -S_{21} E_x \ \text{ and } \ \nu_{yx} = -S_{12} E_y \tag{9}$$

The main purpose of this section is to determine the effective constitutive constants of the couple-stress continuum from the WOA response of random fibrous networks. We design different boundary conditions for the determination of the independent components of the constitutive (rigidity) constants over a WOA domain Ω with boundary $\partial\Omega$. The network has no thickness, and in each case, we force the WOA to bear the designed specific deformation $\{\epsilon_{xx}, \epsilon_{yy}, \epsilon_{xy}, \kappa_{xz}, \kappa_{yz}\}^T$ and compute numerically the total elastic strain energy $\mathcal{W}_{WOA}$ stored in the WOA under the corresponding boundary conditions. The numerical procedure used here is similar to that used in [37] but restricted to 2D situation : the total strain energy stored in the WOA is required to be equal to the energy of an equivalent homogeneous couple-stress continuum, thus

$$\mathcal{W}_{WOA} = \mathcal{W}_{\text{couple-stress}} = \frac{1}{2} \cdot a \cdot [\epsilon_{ij} A_{ijkl} \epsilon_{kl} + \kappa_{ij} D_{ijkl} \kappa_{kl}] \tag{10}$$

where a is the area of the WOA. The strain energy stored in the effective homogeneous couple-stress continuum can be obtained by the prescribed strain–stress fields. The effective properties are obtained based on the response of the WOA under prescribed boundary conditions. Kinematic boundary conditions are applied on part of the WOA boundary, while free surface boundary conditions are applied on complementary surfaces. In a recent work [47], it is found that the analysis using this kind of boundary conditions leads to classical and couple-stress moduli which are, respectively, independent and dependent on the size of the WOA. In order to evaluate the components of the couple-stress stiffness tensors $\mathbf{A}$ and $\mathbf{D}$ for the WOA, we conduct the following six elementary tests :

The first following four tests are constructed to determine the stiffness matrix $\mathbf{A}$.

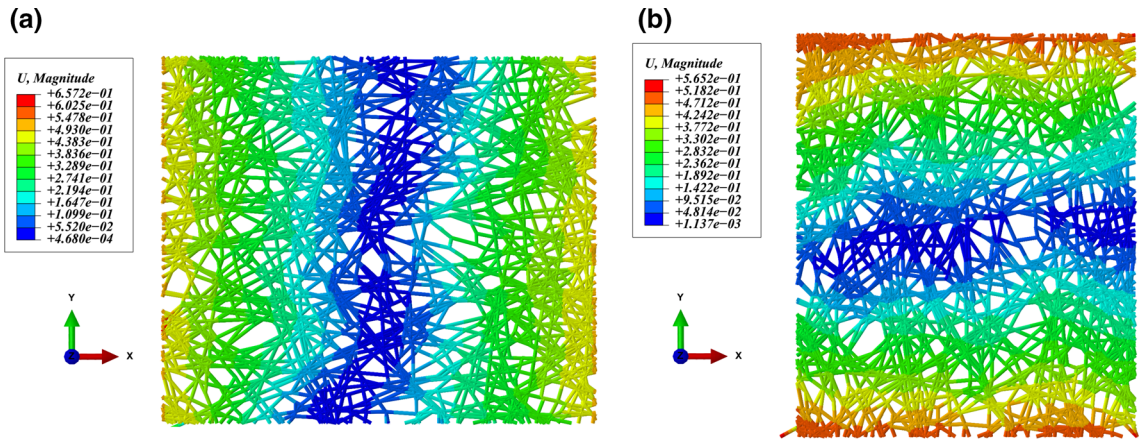

Fig. 3 Displacement fields corresponding to boundary conditions applied to identify the effective constitutive coefficients **a** A_{11} and **b** A_{22}

Test 1: Horizontal uniaxial extension test for A_{11} (Fig. 3a): when we apply a uniform strain $\epsilon_{xx} = 1$ and shear stress $\sigma_{xy} = 0$ on the WOA's boundary, the corresponding boundary conditions are then written as

$$\begin{array}{l} u = x,\ t_y = \sigma_{xy} n_x = 0 \text{ on } n_x \text{ face} \\ v = 0,\ t_x = \sigma_{xy} n_y = 0 \text{ on } n_y \text{ face} \end{array} \tag{11}$$

It gives

$$A_{11} = \frac{2\mathcal{W}_{WOA}}{a} \tag{12}$$

Test 2: Vertical uniaxial extension test for A_{22} (Fig. 3b): when we apply a uniform strain $\epsilon_{yy} = 1$ and shear stress $\sigma_{xy} = 0$ on the WOA's boundary, the corresponding boundary conditions are then written as

$$\begin{array}{l} u = 0,\ t_y = \sigma_{xy} n_x = 0 \text{ on } n_x \text{ face} \\ v = y,\ t_x = \sigma_{xy} n_y = 0 \text{ on } n_y \text{ face} \end{array} \tag{13}$$

It gives

$$A_{22} = \frac{2\mathcal{W}_{WOA}}{a} \tag{14}$$

Test 3: Biaxial extension test for A_{12} (Fig. 4a): when we apply a uniform strain $\epsilon_{xx} = \epsilon_{yy} = 1$ and shear stress $\sigma_{xy} = 0$ on the WOA's boundary, the corresponding boundary conditions are then written as

$$\begin{array}{l} u = x,\ t_y = \sigma_{xy} n_x = 0 \text{ on } n_x \text{ face} \\ v = y,\ t_x = \sigma_{xy} n_y = 0 \text{ on } n_y \text{ face} \end{array} \tag{15}$$

It gives

$$A_{12} = \frac{1}{2}\left(\frac{2\mathcal{W}_{WOA}}{a} - A_{11} - A_{22}\right) \tag{16}$$

Test 4: Shear deformation test for A_{33} (Fig. 4b): when we apply a uniform shear strain $\epsilon_{xy} = 1$ and normal stress $\sigma_{xx} = \sigma_{yy} = 0$ on the WOA's boundary, the corresponding boundary conditions are then written as

$$\begin{array}{l} u = y/2,\ t_y = \sigma_{yy} n_y = 0 \text{ on } n_y \text{ face} \\ v = x/2,\ t_x = \sigma_{xx} n_x = 0 \text{ on } n_x \text{ face} \end{array} \tag{17}$$

It gives

$$A_{33} = \frac{2\mathcal{W}_{WOA}}{a} \tag{18}$$

In order to evaluate the components of the stiffness matrix **D**, the following two bending tests are performed:

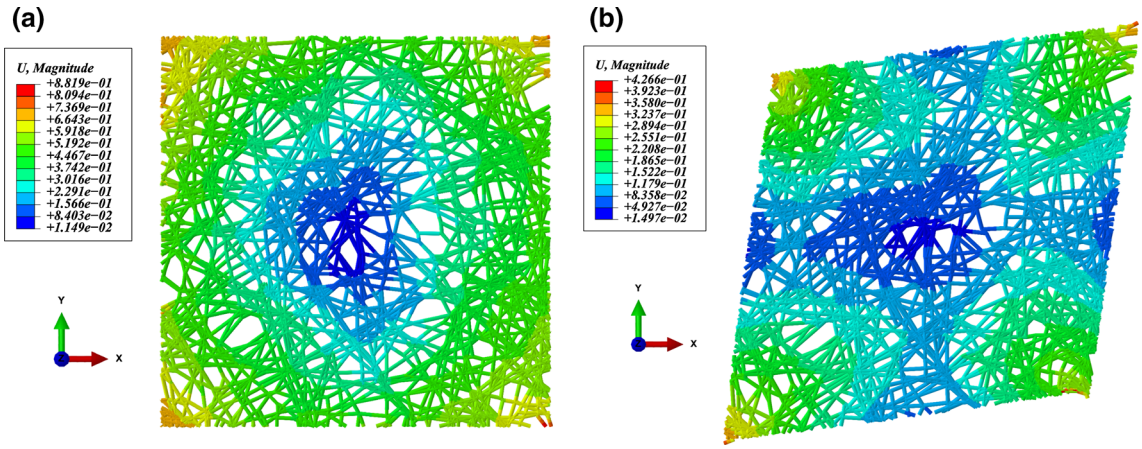

Fig. 4 Displacement fields corresponding to boundary conditions applied to identify the effective constitutive coefficients **a** A_{12} and **b** A_{33}

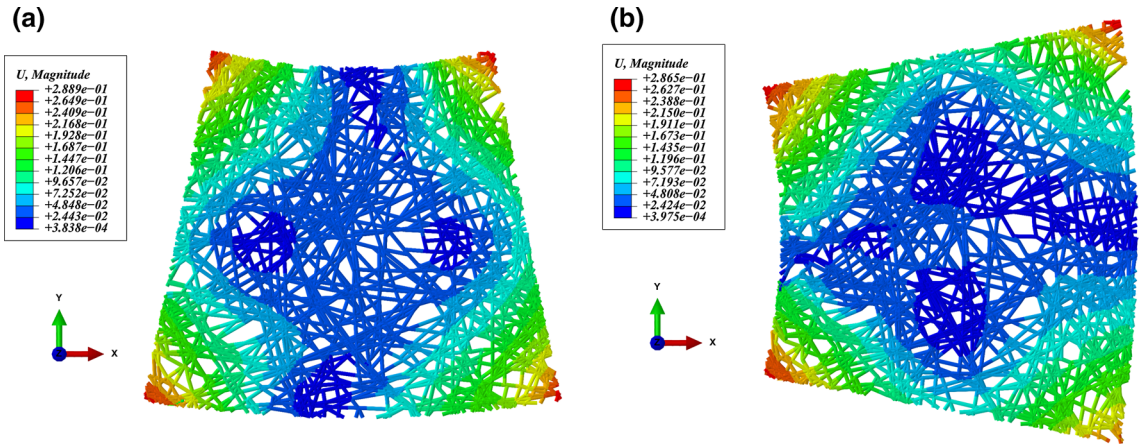

Fig. 5 Displacement fields corresponding to boundary conditions applied to identify the effective constitutive coefficients **a** D_{11} and **b** D_{22}

Test 5: Uniform curvature test for D_{11} (Fig. 5a): when we apply a uniform bending curvature $\kappa_{xz} = 1$ on the WOA's boundary, the corresponding boundary conditions are then written as

$$\begin{aligned} u &= -xy \text{ on } n_x \text{ face} \\ v &= x^2/2 \text{ on } n_y \text{ face} \end{aligned} \tag{19}$$

It gives

$$D_{11} = \frac{2\mathcal{W}_{WOA}}{a} \tag{20}$$

Test 6: Uniform curvature test for D_{22} (Fig. 5b): when we apply a uniform bending curvature $\kappa_{yz} = 1$ on the WOA's boundary, the corresponding boundary conditions are then written as

$$\begin{aligned} u &= -y^2/2 \text{ on } n_x \text{ face} \\ v &= xy \quad \text{ on } n_y \text{ face} \end{aligned} \tag{21}$$

It gives

$$D_{22} = \frac{2\mathcal{W}_{WOA}}{a} \tag{22}$$

Since the characteristic length is an essential parameter in the couple-stress continua, we generalize the definition of this parameter to an anisotropic continuum in terms of the engineering constants. Two characteristic

lengths can be extracted from the micropolar constitutive law, corresponding to the bending or torsion couple-stress components. The characteristic lengths are identified from the homogenized stiffness matrix components as [47]:

$$l_{mx} = \left(\frac{D_{11}}{4A_{33}}\right)^{\frac{1}{2}}; \quad l_{my} = \left(\frac{D_{22}}{4A_{33}}\right)^{\frac{1}{2}} \tag{23}$$

In random networks, the fibers are considered as beam elements and are characterized by stretching, bending and shear rigidities, expressed by parameters $\eta = E_f A$, $k = E_f I$ and $\gamma = \lambda G_f A$. Parameters A and I therein are the area and moment of inertia of the fiber cross section, E_f is the fiber Young's modulus, G_f is the fiber shear modulus, and λ is a constant equal to 0.88 (for beams with a circular cross section). We note that in random fiber networks with random orientation of fibers, the distribution of segment length is a Poisson process with an average $l_c = \pi/2\rho$ where ρ is the network density with dimensions of [length]$^{-1}$[44]. However, a large number of short fiber segments appear in the networks and the Euler–Bernoulli model loses accuracy [50]; this is why we prefer the Timoshenko beam model [51] that gives more accurate predictions for short, stubby beams, although both models give the same predictions for long, slender beams.

In addition to the characteristic lengths of the system noted above, which depend on the geometry of the fiber network, one shall introduce another characteristic length that depends on the mechanical properties of individual fibers and quantifies the relative importance of bending versus stretch; this characteristic length is elaborated from the bending and stretching stiffnesses, parameters k and η, respectively, as $l_b = (k/\eta)^{1/2}$. This parameter plays an important role especially in quantifying the relative importance of bending effects of the fibers in determining the dominant deformation mode of the network. We study the effect of fiber bending length, network density, window size and the nature of fiber–fiber joints on the overall mechanical behavior of the material. The total energy of the system is computed numerically as the sum of all strain energies associated with bending, stretching and shear deformation, i.e.,

$$\mathcal{W}_{WOA} = \frac{1}{2} \sum_{fibers} \int_0^{L_0} \left[k \left(\frac{d\psi}{ds}\right)^2 + \eta \left(\frac{du}{ds}\right)^2 + \gamma \left(\frac{dv}{ds} - \psi\right)^2 \right] ds \tag{24}$$

In expression (24), $\psi(s)$ the rotation of plane normal to the neutral axis of the beam. $v(s)$ represents the transverse displacement, and $\frac{du(s)}{ds}$ is the axial strain at position s along the fiber. The rotation of the fiber cross section is $\frac{dv(s)}{ds}$, while the difference $\frac{dv(s)}{ds} - \psi(s)$ represents the transverse shear deformation of the beam. The numerical homogenization technique consists in determining the overall effective mechanical properties (couple-stress moduli and characteristic lengths) over a WOA of the random network using finite element discretization of the WOA geometry. Each fiber segment is modeled as a three-node beam element (element type B22 in ABAQUS), endowed with bending, stretching and shearing deformation mechanisms.

4 Justification of the construction of a couple-stress model for random fiber networks

The goal of this section is to justify the construction of couple-stress type generalized continuum models through both analytical and numerical approaches. Motivations for adopting an effective couple-stress model shall be provided by computing a closed-form solution of a tensile test and comparing with the response of the same domain predicted by fully resolved FE computations; in a second step, we shall determine the bending response of a macrobeam incorporating a random microstructure based on the homogenized couple-stress moduli and also compare the effective bending modulus with the one predicted by FE analysis over the full network.

4.1 Analytical approach

We consider the model problem of the uniaxial traction (Fig. 6) of an initially homogeneous plate, the material behavior of which being modeled by a couple-stress continuum, with effective properties reflecting those of a random fibrous underlying microstructure. We shall compare the local microrotation fields of the random fiber networks real microstructures with the ones that develop within the homogeneous plate endowed with the effective couple-stress properties of the same random fiber networks in the affine deformation regime.

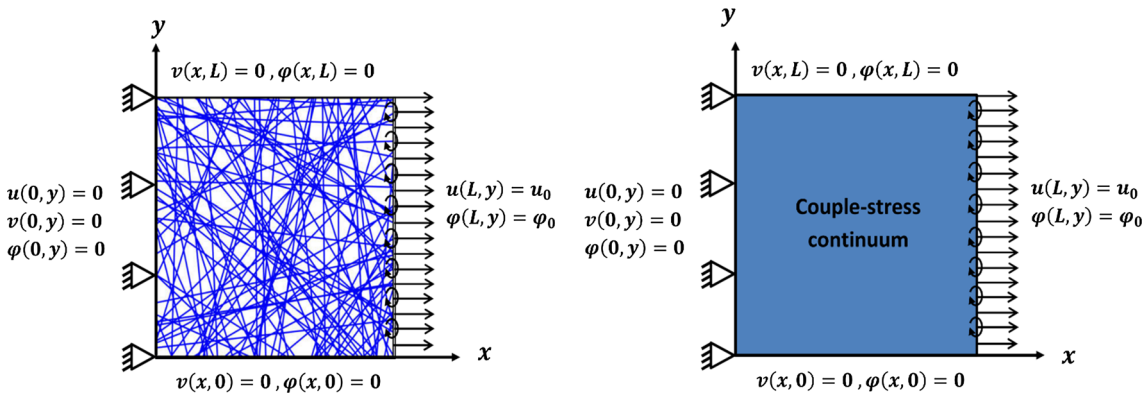

Fig. 6 Random fiber networks and homogeneous plate subjected to the same boundary conditions for a simple traction test

The microrotations are supposed nil on the top, bottom and left edges of the plate, simulating a simple traction of a couple-stress continuum. Our interest here is to find a bivariate solution with respect to x and y of the rotation function $\phi(x, y)$ and the kinematic measures $\kappa_{xz}(x, y) = \frac{\partial \phi}{\partial x}$ and $\kappa_{yz}(x, y) = \frac{\partial \phi}{\partial y}$. The degrees of freedom and the strain components are presented in Sect. 3 and are recalled here in index notation as

$$\varepsilon_{ij} = u_{i,j} + \epsilon_{ijk}\phi_k, \quad \kappa_{ij} = \phi_{i,j} \ \text{ with } \ \phi_k = \epsilon_{ijk}u_{j,i}/2 \tag{25}$$

The displacement and microrotation field are sought in a general form as two functions depending on x and y

$$\boldsymbol{u} = u(x, y) \cdot \boldsymbol{e_x} + v(x, y) \cdot \boldsymbol{e_y} \ \text{ and } \ \boldsymbol{\phi} = \phi(x, y) \cdot \boldsymbol{e_z} \tag{26}$$

These analyses entail the following strain and microcurvature tensors

$$[\varepsilon] = \begin{pmatrix} \frac{\partial u}{\partial x} & \frac{\partial v}{\partial x} - \phi & 0 \\ \frac{\partial u}{\partial y} + \phi & \frac{\partial v}{\partial y} & 0 \\ 0 & 0 & 0 \end{pmatrix} \text{ and } [\kappa] = \begin{pmatrix} 0 & 0 & 0 \\ 0 & 0 & 0 \\ \frac{\partial \phi}{\partial x} & \frac{\partial \phi}{\partial y} & 0 \end{pmatrix} \tag{27}$$

The couple-stress constitutive laws are given by the following relations between the stress, couple stress, strain and curvature tensors

$$\begin{aligned} \boldsymbol{\sigma} &= \lambda[\mathbf{tr}(\boldsymbol{\varepsilon})]\mathbf{1} + 2\mu\boldsymbol{\varepsilon} \\ \boldsymbol{m} &= \alpha[\mathbf{tr}(\boldsymbol{\kappa})]\mathbf{1} + 2\beta\boldsymbol{\kappa} \end{aligned} \tag{28}$$

Inserting thereabove the definition of the kinematic variables based on Eqs. (25) and (26) leads to the following expression of the stress and couple-stress components

$$\begin{aligned} \sigma_{xx} &= (\lambda + 2\mu)\frac{\partial u}{\partial x} + \lambda\frac{\partial v}{\partial y} \\ \sigma_{xy} &= 2\mu\left(\frac{\partial v}{\partial x} - \phi\right) \\ \sigma_{yx} &= 2\mu\left(\frac{\partial u}{\partial y} + \phi\right) \\ \sigma_{yy} &= \lambda\frac{\partial u}{\partial x} + (\lambda + 2\mu)\frac{\partial v}{\partial y} \\ m_{xz} &= 2\beta\frac{\partial \phi}{\partial x} \\ m_{yz} &= 2\beta\frac{\partial \phi}{\partial y} \end{aligned} \tag{29}$$

These expressions are next inserted into equilibrium equations (4), leading in turn to the following two PDEs for the three unknown kinematic variables

$$(\lambda + 2\mu)\left(\frac{\partial^2 u}{\partial x^2} + \frac{\partial^2 u}{\partial x \partial y}\right) + (\lambda + 2\mu)\left(\frac{\partial^2 v}{\partial y^2} + \frac{\partial^2 v}{\partial x \partial y}\right) + 2\mu\left(\frac{\partial \phi}{\partial x} - \frac{\partial \phi}{\partial y}\right) = 0 \tag{30}$$

$$\frac{\partial^2 \phi}{\partial x^2} + \frac{\partial^2 \phi}{\partial y^2} = 0 \tag{31}$$

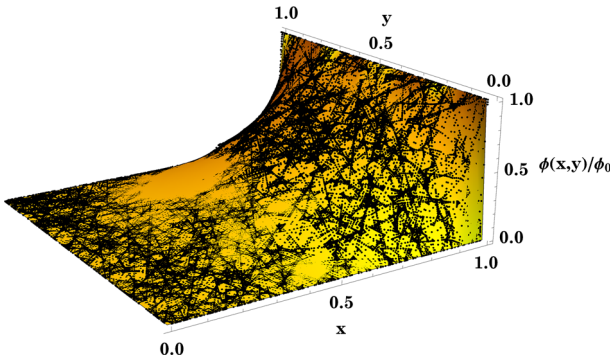

Fig. 7 Comparison between analytical (continuous surface) and microstructural (black points) solutions of the normalized microrotations field $\phi(x, y)/\phi_0$. The window of analysis is selected to be of unit size, $L = 1$

By the method of separation of variables and Fourier analysis, one can determine the solution of the two-dimensional Laplace equation satisfied by the microrotation assuming that the solution can be written in the following separated form

$$\phi(x, y) = f(x) \cdot g(y) \tag{32}$$

Using the boundary conditions shown in Fig. 6, we find the analytical solution of the Laplace equation for the microrotation field

$$\frac{\phi}{\phi_0} = \frac{4}{\pi} \sum_{m=1}^{\infty} \frac{1}{(2m-1)\sinh[(2m-1)\pi]} \sinh\left[\frac{(2m-1)\pi x}{L}\right] \sin\left[\frac{(2m-1)\pi y}{L}\right] \tag{33}$$

and for the microcurvatures $\kappa_{xz} = \frac{\partial \phi}{\partial x}$ and $\kappa_{yz} = \frac{\partial \phi}{\partial y}$ as

$$\kappa_{xz} = \frac{4\phi_0}{L} \sum_{m=1}^{\infty} \frac{1}{\sinh[(2m-1)\pi]} \cosh\left[\frac{(2m-1)\pi x}{L}\right] \sin\left[\frac{(2m-1)\pi y}{L}\right] \tag{34}$$

$$\kappa_{yz} = \frac{4\phi_0}{L} \sum_{m=1}^{\infty} \frac{1}{\sinh[(2m-1)\pi]} \sinh\left[\frac{(2m-1)\pi x}{L}\right] \cos\left[\frac{(2m-1)\pi y}{L}\right] \tag{35}$$

The microrotation field predicted by the analytical solution of the effective couple-stress continuum and the predictions of the fully resolved microstructural computations over the random fiber networks is in good agreement, as shown in Fig. 7. This provides a first justification of the employed couple-stress substitution medium.

4.2 Microstructural impact of the random microstructure on the effective bending rigidity

Based on the homogenized properties of the random fiber networks computed in Sect. 3 we will quantify the effects of the couple-stress model on the macroscopic scale. We shall thereby compare the simplified equation of a micropolar beam incorporating random fibers under pure bending to the standard bending equations of classical beam theory. The geometrical parameters of the macrobeam are indicated in Fig. 8 with h the beam height.

The bending response of an elastic beam subjected to a uniform bending moment M reads based on couple-stress theory as

$$(E_x I_z + D_{11} h)\frac{\partial \phi}{\partial x} = -M \quad \text{and} \quad (E_y I_z + D_{22} h)\frac{\partial \phi}{\partial y} = -M \tag{36}$$

with E_x and E_y the effective Young's moduli of the macroscopic beam, M the bending moment, I_z the quadratic moment of the macroscopic beam along z and $\kappa^{xz}_{\text{couple-stress}} = E_x I_z + D_{11} h$, $\kappa^{yz}_{\text{couple-stress}} = E_y I_z + D_{22} h$ the bending stiffnesses of the beam exhibiting couple-stress effect. The macroscopic parameter h is the height

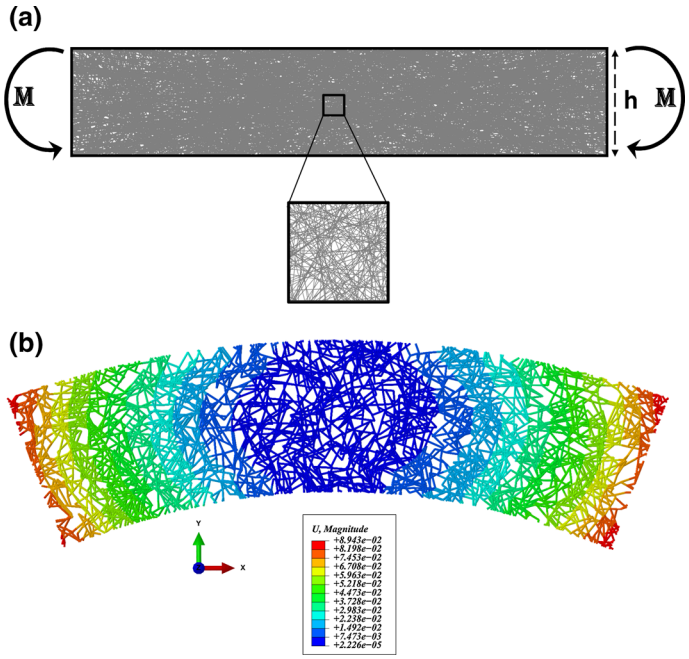

Fig. 8 **a** A macroscopic beam with random fibers subjected to pure bending and **b** iso displacement for the bending of the macrobeam in (mm)

of the random fiber structure which is taken as 2 mm (Fig. 8). Equation (36) shows that in addition to the couple-stress moduli D_{11} and D_{22}, there is a geometrical effect impacting the overall beam bending rigidity via parameter h.

On the other hand if we exclude the couple-stress effects, the classical bending stiffnesses, $\kappa^{xz}_{\text{classical}}$ and $\kappa^{yz}_{\text{classical}}$, for a homogeneous equivalent beam are defined by the following relations

$$(E_x I_z)\frac{\partial \phi}{\partial x} = -M \quad \text{and} \quad (E_y I_z)\frac{\partial \phi}{\partial y} = -M \tag{37}$$

The difference between the bending rigidities of the homogenized beam calculated based on Cauchy and couple-stress theories is elaborated as the following scalar parameter expressed in percentage

$$g_b = \frac{\kappa_{\text{couple-stress}} - \kappa_{\text{classical}}}{\kappa_{\text{couple-stress}}} \cdot 100 \tag{38}$$

The gain in flexural rigidity g_b for the couple-stress continuum in the ADR and NADR is, respectively, 89% and 94%; these numbers are validated by microstructural computations performed over the entire (discrete) random microstructure, giving, respectively, rigidity increases of 90% and 93%. The gain in flexural rigidity predicted by the equivalent couple-stress model and by fully resolved random fiber networks computations has comparable values, close to 90%, thus evidencing that the random fiber microstructure has a significant impact on the bending behavior at the macrolevel. The strong impact of bending effects of the fibers at the macroscopic level motivates the use of a couple-stress continuum in which the overall bending response is captured by the microrotation and the resulting microcurvatures.

5 Effect of random fiber networks main parameters on the effective moduli

5.1 Effect of fiber bending length l_b

The effective elastic moduli depend strongly on the competition between energy storage in the bending and axial modes quantified by parameter l_b; we accordingly investigate the effect of l_b on the classical and couple-stress elastic constants. The effect of l_b on the classical elastic constants has been discussed extensively in the literature [18,52–54] and is presented here as a matter of reference.

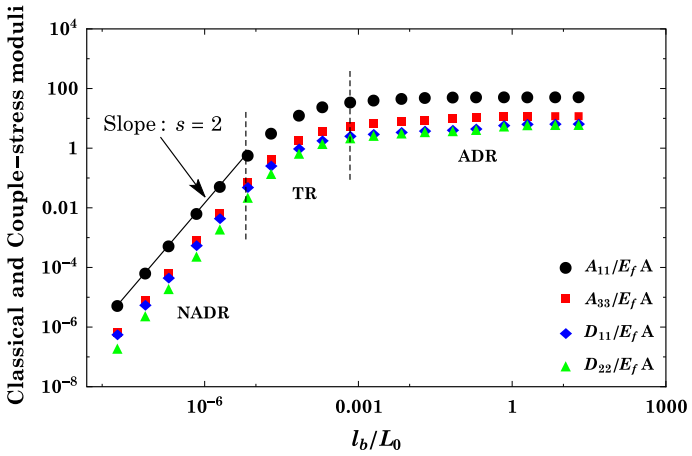

Fig. 9 Evolution of classical and couple-stress moduli versus the normalized fiber bending length l_b/L_0 with normalized network density $\rho L_0 = 75$

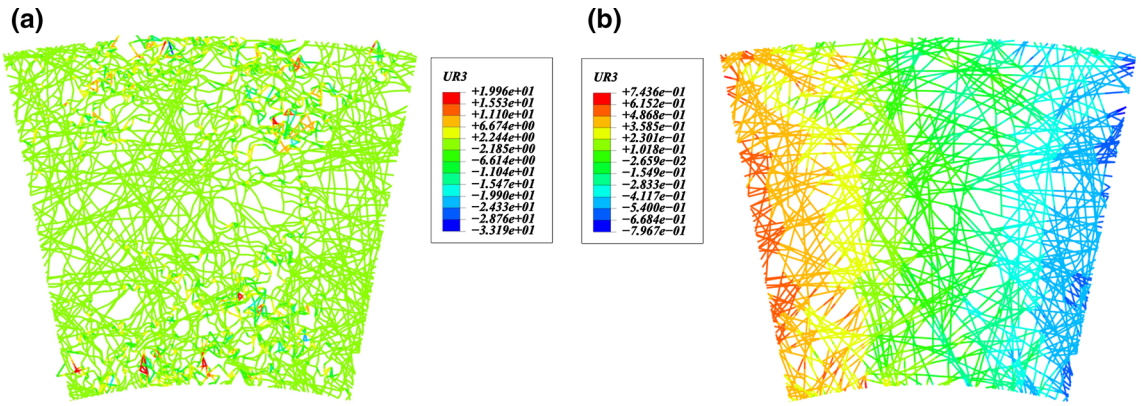

Fig. 10 Microrotation fields for both deformation regimes. **a** Non-affine deformation regime (NADR) $l_b/L_0 = 2 \times 10^{-5}$ and **b** affine deformation regime (ADR) $l_b/L_0 = 2 \times 10^{-2}$

We tune the fiber bending length by changing the fiber diameter, which in turn affects the area and moment of inertia of the fibers. We represent in Fig. 9 in logarithmic axes the evolution of two among the four classical moduli (A_{11} and A_{33}) normalized by $E_f A$ versus the fiber bending length normalized by the fiber length L_0. The network density is kept constant in all computations such that $\rho L_0 = 75$. The values obtained for A_{22} match those reported in Fig. 9 for A_{11} (although not shown here), while A_{12} follows closely A_{33}. Note that the variable on the horizontal axis is proportional to the aspect ratio of fibers.

The same trend is observed for all classical moduli. For low values of normalized bending length we observe that the classical moduli are proportional to $E_f A l_b^2$ which is equal to $E_f I$, and strain energy is stored predominantly in the bending mode: this is the non-affine deformation regime (abbreviated as NADR). This is followed by a transition zone toward the affine deformation regime (abbreviated as ADR) for large values of l_b/L_0 in which the classical moduli are proportional to $E_f A$ and the strain energy is stored predominantly in the axial deformation mode of fibers. The vertical dashed lines shown in Fig. 9 define the approximate limits of the NADR and ADR regimes. The transition region is defined as the intermediate region separating the affine and non-affine behaviors.

In the same figure (Fig. 9), we show the evolution of normalized couple-stress moduli versus the normalized fiber bending length. Interestingly, the couple-stress moduli exhibit the same behavior as the classical moduli. Furthermore, the transition from ADR to NADR takes place in the same range of the ratio l_b/L_0. The spatial distribution of the local microrotation field at the scale of individual fibers computed by FE shown in Fig. 10 has clearly a much higher amplitude in the non-affine regime compared to the affine regime. The mesoscopic microrotation represents in some sense the averaging of the individual fiber rotations.

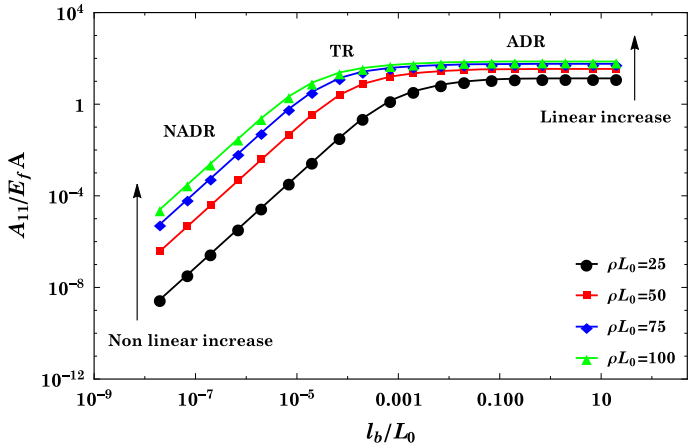

Fig. 11 Evolution of stretching modulus versus the normalized fiber bending length l_b/L_0 and different densities ρL_0

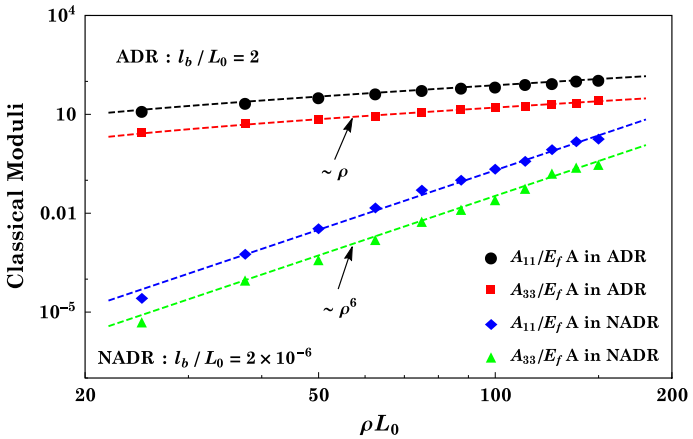

Fig. 12 Evolution of classical moduli versus normalized network density ρL_0 in both affine (ADR) and non-affine (NADR) deformation regimes with $l_b/L_0 = 2$ and $l_b/L_0 = 2 \times 10^{-6}$, respectively

The elastic modulus A_{11} shows a linear dependence on network density ρ in the affine regime and a nonlinear dependence on ρ in the non-affine regime, as shown in Fig. 11. The transition from the non-affine to the affine regime occurs later for lower densities. A similar effect of network density on the evolution of the couple-stress moduli is observed, and the bending moduli increases with network density over all the range of densities. As with the case of classical moduli, we observe that the affine regime is reached at an early stage for high densities. In order to refine these tendencies, we record in the following section the evolution of the classical and couple-stress moduli versus normalized network density, in both the affine and non-affine regimes.

5.2 Effect of network density ρ

We evaluate the classical and non-classical moduli versus the normalized network density parameter, ρL_0 (we recall that the network density is defined as the total fiber length per unit area), focusing on the affine deformation regime. The classical moduli are linearly related to density, as shown in Fig. 12; both tensile moduli vary linearly with respect to density with a similar slope, which is higher than the slope of the linear evolution of the shear and biaxial moduli versus density.

We also evaluate the relation between classical moduli and the normalized network density for small values of l_b/L_0 (NADR) and observe a nonlinear relation between the two. In this regime too, the biaxial and shear moduli are lower than the tensile moduli. We observe that the classical moduli are proportional to ρ^6 over all

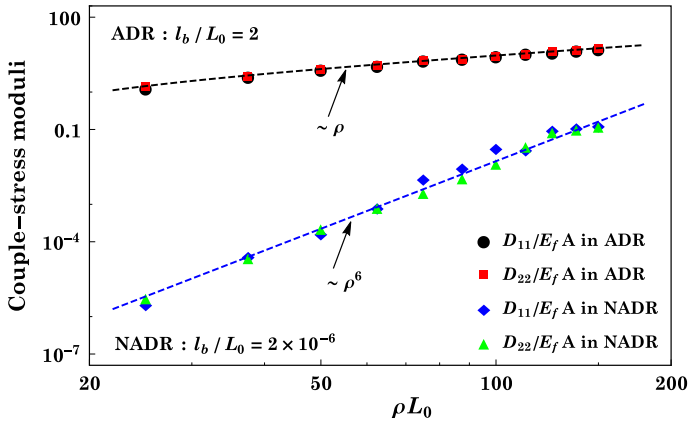

Fig. 13 Variation of couple-stress moduli versus normalized network density ρL_0 in both affine (ADR) and non-affine (NADR) deformation regimes with $l_b/L_0 = 2$ and $l_b/L_0 = 2 \times 10^{-6}$, respectively

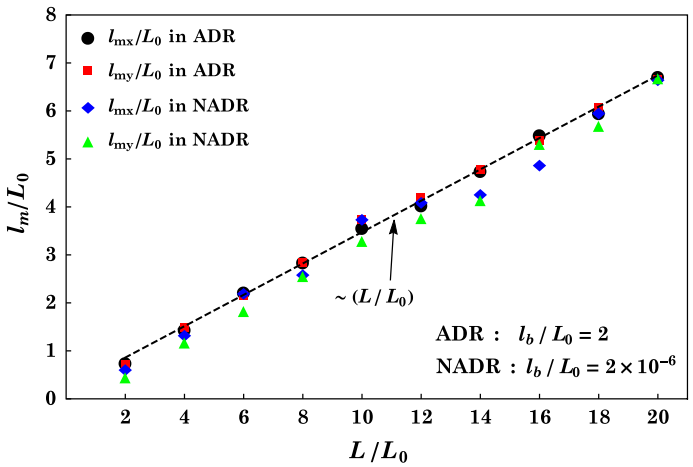

Fig. 14 Variation of l_m/L_0 versus normalized window size L/L_0 in both affine (ADR) and non-affine (NADR) deformation regimes with $l_b/L_0 = 2$ and $l_b/L_0 = 2 \times 10^{-6}$, respectively

range of densities for $l_b/L_0 = 2 \times 10^{-6}$. Similar plots of the bending moduli of the couple-stress continuum versus normalized network density are obtained in both affine (ADR) and non-affine (NADR) deformation regimes, as shown in Fig. 13.

5.3 Effect of window size L

The dependence of the classical moduli on the size of the model is discussed in detail in [18]. The size effect is associated with the randomness of the structure and the stochasticity of the deformation field. Since higher spatial fluctuations are observed in NADR as compared to ADR, the size effect shall be more pronounced in the NADR regime. This trend is indeed observed for the classical moduli and a method to predict the size for which a model becomes representative (size effect free) for any value of the model parameters (ρ, l_b) has been proposed in [18]. In the present study, we use this method and consider only models of size L large enough to avoid the size effect of the classical moduli. For such networks, we inquire whether the couple-stress moduli are affected by the size of the model.

The micropolar bending lengths quantify the extent of microstructural interactions due to fiber bending, at the mesoscopic level of description. The mesoscopic bending length l_m defined in Eq. (23) is shown to increase linearly with the window size, in both the affine and non-affine regimes, as illustrated in Fig. 14, while keeping the normalized network density constant $\rho L_0 = 25$. Thus, size effects scale linearly with the window size and cannot be eliminated in both affine and non-affine deformation regimes

6 Conclusion and future directions

Random fibrous networks define the microstructure of many artificial or biological materials, including paper, biological gels and collagenous networks forming biological tissues. It is challenging to identify an effective constitutive law for such materials due to the complex fiber–fiber interactions and the additional length scales introduced due to the network structure. This motivates the search for suitable effective continuum substitution media, with effective mechanical properties related to the microstructural parameters in a quantitative manner. The mechanics of generalized continua have been considered in this contribution to analyze the mechanical response of two-dimensional random fibrous media, accounting for microstructural and scale effects. Effective couple-stress continuum models have been constructed numerically, and the classical and couple-stress moduli have been identified by equating the strain energy evaluated numerically over different windows of analyses and the strain energy of the homogeneous couple-stress substitution medium. The influence of important network parameters, namely the fiber bending length, network density and size of WOA, on the computed effective mechanical moduli has been analyzed.

The network deforms non-affinely for low values of the fiber bending length l_b and affinely for high values of l_b. The classical and couple-stress moduli are proportional to $E_f A$ for higher l_b, hence the deformation is dominated by fiber stretch, whereas these moduli are proportional to $E_f I$ for lower l_b, showing a predominant bending deformation mode. The computations have highlighted a strong size effect, which seem to be unavoidable for such random fibrous media whatever the fiber length (relative to window size). This could mean that a more refined model than couple-stress theory is needed to capture the complex state of deformation and stress within the network.

Such homogenized-based enhanced continuum models developed at the mesoscopic scale of windows of analysis pave the way toward efficient numerical simulations of the mechanical response of stochastic fibrous structures submitted to complex loadings. Future developments shall include the consideration of large deformations leading to effective hyperelastic models and a viscoelastic behavior of fibers.

References

1. Fratzl, P.: Collagen: Structure and Mechanics (Springer, Max Planck Institute of Colloids and Interfaces, Department of Biomaterials, 14424 Potsdam, Germany, 2008)
2. dell'Isola, F., Lekszycki, T., Pawlikowski, M., Grygoruk, R., Greco, L.: Designing a light fabric metamaterial being highly macroscopically tough under directional extension: first experimental evidence. Zeitschrift für angewandte Mathematik und Physik **66**(6), 3473 (2015)
3. Placidi, L., Barchiesi, E., Turco, E., Rizzi, N.: A review on 2D models for the description of pantographic fabrics. Zeitschrift für angewandte Mathematik und Physik **67**, 121 (2016)
4. Dell'Isola, F., Steigmann, D., Corte, A.: Synthesis of fibrous complex structures: designing microstructure to deliver targeted macroscale response. Appl. Mech. Rev. **67**, 060804 (2016)
5. Steigmann, D., dell'Isola, F.: Mechanical response of fabric sheets to three-dimensional bending, twisting, and stretching. Acta Mechanica Sinica **31**(3), 373 (2015)
6. Cox, H.: The elasticity and strength of paper and other fibrous materials. J. Appl. Phys. **3**, 72 (1952)
7. Petterson, D.R.: Mechanics of nonwoven fabrics. J. Ind. Eng. Chem. **51**(8), 902 (1959)
8. Wu, X., Dzenis, Y.A.: Elasticity of planar fiber networks. J. Appl. Phys. **98**, 093501 (2005)
9. MacKintosh, F., Kas, J., Jamney, P.: Elasticity of semiflexible biopolymer networks. Phys. Rev. Lett. **75**, 4425 (1995)
10. Wilhelm, J., Frey, E.: Elasticity of stiff polymer networks. Phys. Rev. Lett. **91**(10), 1 (2003)
11. Palmer, J., Boyc, M.: Constitutive modeling of the stress strain behavior of F-actin filament networks. Acta Biomaterialia **4**(3), 597 (2008)
12. Lee, Y., Jasiuk, I.: Apparent elastic properties of random fiber networks. Comput. Mater. Sci. **79**, 715 (1995)
13. Turco, E., Dell'Isola, F., Cazzani, A., Rizzi, N.: Hencky-type discrete model for pantographic structures: numerical comparison with second gradient continuum models. Zeitschrift für angewandte Mathematik und Physik **67**, 85 (2016)
14. Alibert, J., Corte, A., Giorgio, I., Battista, A.: Extensional Elastica in large deformation as Gamma-limit of a discrete 1D mechanical system. Zeitschrift für angewandte Mathematik und Physik **68**, 42 (2017)
15. DeMasi, A., Olla, S.: Quasi-static hydrodynamic limits. J. Stat. Phys. **61**(5), 1037 (2015)
16. Berrehili, Y., Marigo, J.J.: The homogenized behavior of unidirectional fiber-reinforced composite materials in the case of debonded fibers. Math. Mech. Complex Syst. **2**(2), 181 (2014)
17. Picu, R.C.: Mechanics of random fiber networks-a review. Soft Matter. **7**, 6768 (2012)
18. Shahsavari, A., Picu, R.: Size effect on mechanical behavior of random fiber networks. Int. J. Solids Struct. **50**, 3332 (2013)
19. Astrom, J.A., Makinen, J.P., Alava, M.J., Timonen, J.: Elasticity of planar fiber networks. Phys. Rev. E **61**, 5550 (2000)
20. Hatami-Marbini, H., Picu, R.C.: An eigenstrain formulation for the prediction of elastic moduli of defective fiber networks. Eur. J. Mech. A Solids **28**, 305 (2009)

21. Hatami-Marbini, H., Picu, R.C.: Scaling of nonaffine deformation in random semiflexible fiber networks. Phys. Rev. E **77**, 062103 (2008)
22. Cihan, T., Onck, P.R.: Size effects in two-dimensional Voronoi foams: a comparison between generalized continua and discrete models. J. Mech. Phys. Solids **56**, 3541 (2008)
23. dell'Isola, F., Corte, A., Giorgio, I.: Higher-gradient continua: The legacy of Piola Mindlin, Sedov and Toupin and some future research perspectives. Math. Mech. Solids **22**(4), 852 (2016)
24. Auffray, N., dell'Isola, F., Eremeyev, V., Madeo, A., Rosi, G.: Analytical continuum mechanics ã la Hamilton Piola least action principle for second gradient continua and capillary fluids. Math. Mech. Solids **20**(4), 375 (2013)
25. dell'Isola, F., Andreaus, U., Placidi, L.: At the origins and in the vanguard of peridynamics, non-local and higher-gradient continuum mechanics: an underestimated and still topical contribution of Gabrio Piola. Math. Mech. Solids **20**(8), 887 (2014)
26. Aminpour, H., Rizzi, N.: On the modelling of carbon nano tubes as generalized continua. In: Altenbach, H., Forest, S. (eds.) Generalized Continua as Models for Classical and Advanced Materials, pp. 15–35. Springer, Berlin (2016)
27. Altenbach, H., Eremeyev, V.: On the constitutive equations of viscoelastic micropolar plates and shells of differential type. Math. Mech. Solids **3**(3), 273 (2015)
28. Misra, A., Poorsolhjouy, P.: Grain- and macro-scale kinematics for granular micromechanics based small deformation micromorphic continuum model. Mech. Res. Commun. **21**, 1 (2017)
29. Cosserat, E., Cosserat, F.: Theorie des Corps Deformables. Hermann, Paris (1909)
30. Grioli, G.: Elasticita asimmetrica. Annali di Matematica Pura ed Applicata **50**(1), 389 (1960)
31. Rajagopal, E.S.: The existence of interfacial couples in infinitesimal elasticity. Annalen der Physik **461**(3–4), 192 (1960)
32. Truesdell, C.A., Toupin, R.A.: The Classical Field Theories. Encyclopedia of Physics, III/1. Springer, Berlin (1960)
33. Aero, E.L., Kuvshinskii, E.V.: The main equations of the theory of elastic media with rotationally interacting particles. Fizika Tverdogo Tela **2**, 1399 (1960)
34. Eringen, A.C.: Nonlinear Theory of Continuous Media. McGraw-Hill, New York (1962)
35. Mindlin, R.D., Tiersten, H.F.: Effects of couple stresses in linear elasticity. Arch. Ration. Mech. Anal. **11**, 415 (1962)
36. Koiter, W.T.: Effects of couple stresses in linear elasticity. Proceedings of the Koninklijke Nederlandse Akademie van Wetenschappen, Series B **67**(1), 17 (1964)
37. Goda, I., Ganghoffer, J.F.: Identification of couple-stress moduli of vertebral trabecular bone based on the 3D internal architectures. J. Mech. Behav. Biomed. Mater. **51**, 99 (2015)
38. Misra, A., Poorsolhjouy, P.: Identification of higher-order elastic constants for grain assemblies based upon granular micromechanics. Math. Mech. Solids **3**(3), 285 (2015)
39. Boutin, C., Dell'Isola, F., Giorgio, I., Placidi, L.: Linear pantographic sheets : asymptotic micro–macro models identification. Math. Mech. Complex Syst. **5**(2), 127 (2017)
40. Giorgio, I.: Numerical identification procedure between a micro-Cauchy model and a macro-second gradient model for planar pantographic structures. Zeitschrift für angewandte Mathematik und Physik **67**, 95 (2016)
41. Placidi, L., Andreaus, U., Giorgio, I.: Identification of two-dimensional pantographic structure via a linear D4 orthotropic second gradient elastic model. J. Eng. Math. **103**(1), 1 (2017)
42. Placidi, L., Andreaus, U., Corte, A., Lekszycki, T.: Gedanken experiments for the determination of two-dimensional linear second gradient elasticity coefficients. Zeitschrift für angewandte Mathematik und Physik **66**(6), 3699 (2015)
43. Miles, R.E.: Random polygons determined by random lines in a plane. Proc. Natl. Acad. Sci. USA **52**(4), 901 (1964)
44. Kallmes, O., Corte, H.: The structure of paper. I. The statistical geometry of an ideal two dimensional fiber network. Tappi J. **43**, 737 (1960)
45. Jasiuk, I., Ostoja-Starzewski, M.: Planar Cosserat elasticity of materials with holes and intrusions. Appl. Mech. Rev. **48**(11), 11 (1995)
46. Liu, S., Su, W.: Effective couple-stress continuum model of cellular solids and size effects analysis. Int. J. Solids. Struct. **46**(14–15), 2787 (2009)
47. Goda, I., Assidi, M., Ganghoffer, J.F.: A 3D elastic micropolar model of vertebral trabecular bone from lattice homogenization of the bone microstructure. Biomech. Model. Mechanobiol. **13**(1), 53 (2014)
48. Goda, I., Assidi, M., Belouettar, S., Ganghoffer, J.F.: A micropolar anisotropic constitutive model of cancellous bone from discrete homogenization. J. Mech. Behav. Biomed. Mater. **16**, 87 (2012)
49. Mindlin, R.D.: Micro-structure in linear elasticity. Arch. Ration. Mech. Anal. **16**, 51 (1964)
50. Shahsavari, A., Picu, R.C.: Model selection for athermal cross-linked fiber networks. Phys. Rev. E **86**, 011923 (2011)
51. Gere, J.M., Temoshenko, S.P.: Mechanics of Materials, pp. 02116–4324. PWS Publishing Company, 20 Park Plaza, Boston (1997)
52. Head, D., Levine, A., MacKintosh, F.: Distinct regimes of elastic response and deformation modes of cross-linked cytoskeletal and semiflexible polymer networks. Phys. Rev. E **68**(6), 061907 (2003)
53. Head, D.A., Levine, A.J., MacKintosh, F.C.: Deformation of cross-linked semiflexible polymer networks. Phys. Rev. Lett. **91**(10), 108102 (2003)
54. Wilhelm, J., Frey, E.: Elasticity of stiff polymer networks. Phys. Rev. Lett. **91**(10), 108103 (2003)